Observation of collinear antiferromagnetic domains making use of the circular dichroic charge-magnetic interference effect of resonant x-ray diffraction

Hiroki Ueda,[1,*] Yoshikazu Tanaka,[2] Yusuke Wakabayashi,[1] and Tsuyoshi Kimura[3]

[1]*Division of Materials Physics, Graduate School of Engineering Science, Osaka University, Toyonaka, Osaka 560-8531, Japan*

[2]*RIKEN SPring-8 Center, Sayo, Hyogo 679-5148, Japan*

[3]*Department of Advanced Materials Science, University of Tokyo, Kashiwa, Chiba 277-8561, Japan*

(Received 26 March 2018; revised manuscript received 13 July 2018; published 10 October 2018)

The circular dichroic charge-magnetic interference effect in resonant x-ray diffraction (RXD) is reported for antiferromagnetic (AFM) materials. The polarization dependence of the scattering cross-section was formulated, and the conditions that the interference gives rise to circular dichroic RXD signals for AFM materials were clarified. By using the interference effect, a pair of AFM domains can be distinguished in certain conditions. We applied this effect to observe collinear chirality AFM domains in a high-temperature magnetoelectric hexaferrite, $Ba_{1.3}Sr_{0.7}CoZnFe_{11}AlO_{22}$. Despite its collinear spin arrangement and absence of macroscopic magnetization, the domains are clearly visualized by a circularly polarized x-ray beam. The present result shows that various types of AFM domains including collinear ones can be examined by utilizing the charge-magnetic interference effect, together with the well-established circular dichroism on RXD emerged from pure magnetic scattering.

DOI: 10.1103/PhysRevB.98.134415

I. INTRODUCTION

Antiferromagnetism is defined as ordered magnetism in which the macroscopic magnetization is cancelled out due to the microscopic spin motifs. Recent scientific and technological developments on magnetism enhance the significance of antiferromagnetic (AFM) materials in several topics such as exchange bias [1] and magnetoelectric effect [2]. As in ferromagnetic materials, which possess macroscopic magnetization and are widely used in technological applications, the understanding and the manipulation of magnetic domains in AFM materials are crucial for the above-mentioned functionalities. As illustrated in Fig. 1, four types of AFM domains are known to emerge by symmetry breakings in AFM ordering: (i) configuration domains by translational symmetry breaking [Fig. 1(a)], (ii) orientation domains by rotation symmetry breaking [Fig. 1(b)], (iii) 180° domains by time-reversal symmetry breaking [Fig. 1(c)], and (iv) chirality domains by space-inversion symmetry breaking [Fig. 1(d)] [3–5].

Due to the absence of macroscopic magnetization in AFM materials, most of conventional techniques for the observation of ferromagnetic domains cannot be applied to that of AFM ones. However, several experimental techniques for the observation of AFM domains have been developed to date. For example, the configuration domains have been successfully visualized by photoemission microscope using x-ray magnetic linear dichroism [6,7] and neutron diffraction topography [8]. The orientation domains have been observed by photoemission microscopy using x-ray magnetic linear dichroism [9]. In comparison to the observation of these AFM domains, which give rise to separate magnetic reflections and/or trivial linear-polarization-dependent signals between a pair of domains, other techniques are needed for the observation of 180° domains and chirality domains. A few experimental techniques have been elaborately developed for the observation of these domains so far. The 180° domains have been visualized by polarized neutron diffraction topography [10,11] and optical second harmonic generation [12]. The chirality domains have been also observed by polarized neutron diffraction topography [13], optical second harmonic generation [14], and resonant x-ray microdiffraction [15–17].

Among these techniques, resonant x-ray microdiffraction technique has advantageous merits in terms of (i) high spatial resolution by using light-focusing setup, (ii) element specificity by tuning the energy of photons at the resonance of the focused element, and (iii) selective observation of multiple types of AFM domains with different diffraction conditions. When circularly polarized x-rays are utilized as primary beams, circular dichroic signals in resonant x-ray diffraction (RXD) arise through pure magnetic scattering process in some magnetic materials. The dichroic part in diffracted intensity depends on the sign of spin helicity in their magnetic structure. Thus chirality domains in noncollinear helimagnetic materials have been observed by the RXD technique through pure magnetic scattering [15–17]. However, it is not evident whether a pair of collinear AFM domains between which the local magnetic moments are antiparallel (e.g., 180° domains in a simple ↑↓↑↓ spin arrangement) can be distinguished or not through RXD.

In this paper, we show that "a charge-magnetic interference effect" in RXD is responsible for circular dichroic cross-section of AFM materials. In comparison with the circular dichroism due to the pure magnetic scattering, that due to the interference effect in RXD has been much less discussed so far. Here, we reveal that the interference effect causes the circular dichroic RXD signals even in collinear

*ueda@crystal.mp.es.osaka-u.ac.jp

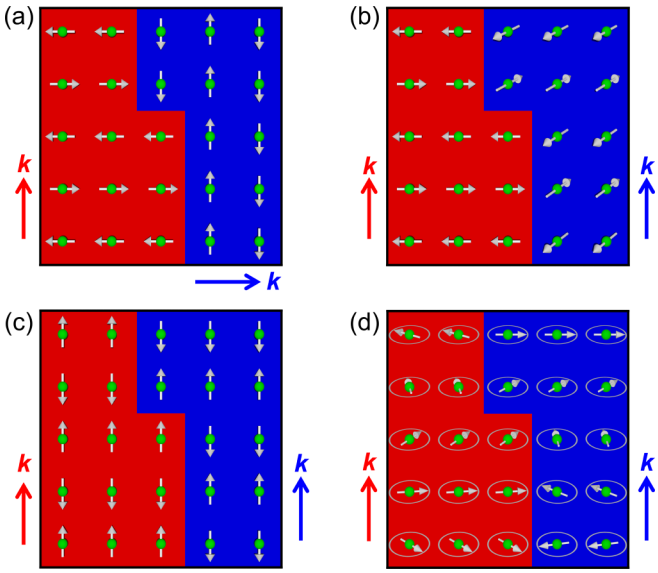

FIG. 1. Schematics of four different antiferromagnetic (AFM) domains: (a) configuration, (b) orientation, (c) 180°, and (d) chirality domains. Here, $\boldsymbol{k}$ is the AFM wave vector in each domain. Green circles and gray arrows denote magnetic atoms and magnetic moments, respectively.

AFM materials. Furthermore, we propose to adopt this effect to the visualization of AFM domain structures in collinear antiferromagnets such as collinear chirality domains in a Y-type hexaferrite, $Ba_{1.3}Sr_{0.7}CoZnFe_{11}AlO_{22}$, showing a high-temperature magnetoelectric effect [18–21].

II. SAMPLE AND EXPERIMENTS

A. Structure and magnetic property of $Ba_{1.3}Sr_{0.7}CoZnFe_{11}AlO_{22}$

Y-type hexaferrites, $(Ba, Sr)_2Me_2Fe_{12}O_{22}$ (Me = divalent transition metal), are nowadays well-known in the field of multiferroics because they often exhibit high-temperature magnetoelectric effects ascribed to their complex spiral magnetic structures stabilized even at room temperature [22]. The crystal structure of Y-type hexaferrite belongs to the space group $R\bar{3}m$ ($a \approx 5.86$ Å and $c \approx 43.4$ Å in the hexagonal setting). Complex magnetic structures in Y-type hexaferrites are generally described by separating the crystal structure into large (L) and small (S) spin blocks, which are alternately stacked along the c axis [Fig. 2(a)]. Most of former studies on the hexaferrites assume that magnetic moments within each block are collinearly aligned [22]. In $Ba_{1.3}Sr_{0.7}CoZnFe_{11}AlO_{22}$ with the Y-type structure, a sharp peak anomaly showing the presence of a magnetic phase transition was seen at $T^* \approx 366$ K in the temperature dependence of magnetization [23], and two types of magnetic satellite peaks, incommensurate $(0\ 0\ 3 \pm \delta)$ [$\delta \approx 0.9$] and commensurate $(0\ 0\ 3 + 1.5)$, were observed in the diffraction profiles at room temperature [18,20]. Based on the approximation of the magnetic structure using the blocks and the presence of two distinct magnetic propagation vectors $\boldsymbol{k}_1 = (0, 0, \delta)$ and $\boldsymbol{k}_2 = (0, 0, 1.5)$, the room-temperature magnetic structure of $Ba_{1.3}Sr_{0.7}CoZnFe_{11}AlO_{22}$ has been discussed in the framework of the so-called alternating longitudinal conical (ALC) structure [Fig. 2(b)]. This magnetic structure is composed of both the in-plane incommensurate helical component shown in Fig. 2(c)

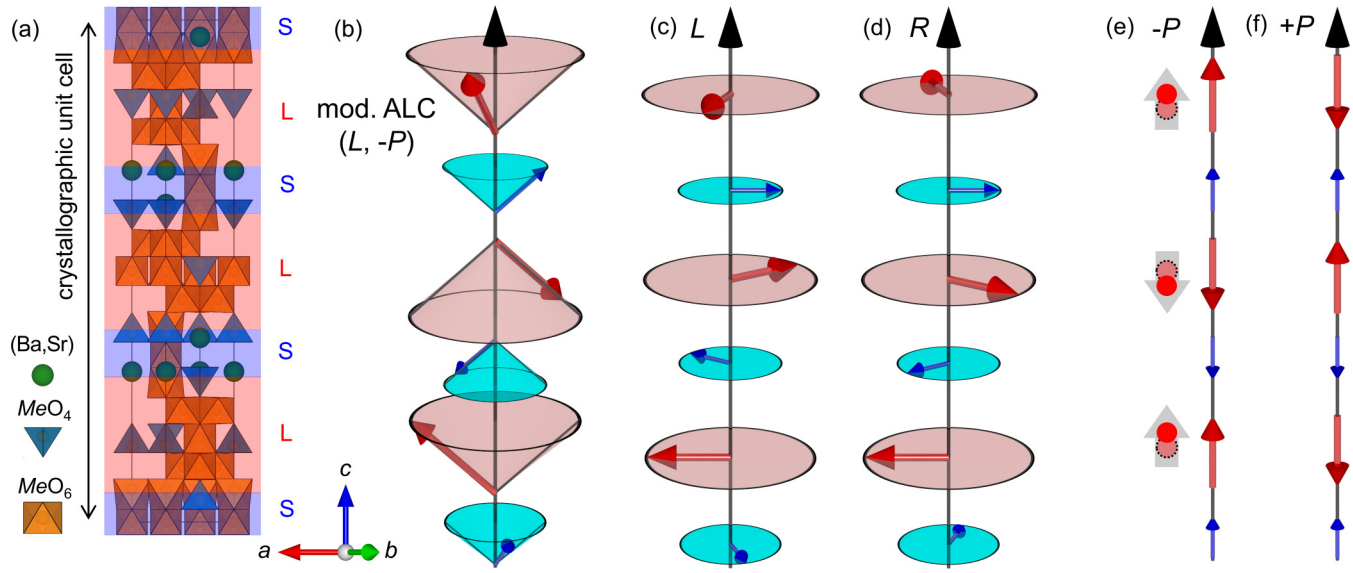

FIG. 2. (a) Crystal structure of $Ba_{1.3}Sr_{0.7}CoZnFe_{11}AlO_{22}$, which is composed of alternating stacks of large (L) and small (S) spin blocks. Here, Me = Fe, Al, Co, and Zn. (b) Revised model of the alternating longitudinal conical (ALC) structure of $Ba_{1.3}Sr_{0.7}CoZnFe_{11}AlO_{22}$. The ALC structure can be divided into two types of the antiferromagnetic (AFM) components illustrated in (c) and (e). The respective AFM components form pairs of helical domain [(c) L and (d) R] and up-up-down-down collinear AFM domain [(e) $-P$ and (f) $+P$]. In the formerly proposed model of the ALC structure [18], the length of blue arrows representing the c-axis component of each magnetic S block in (e) and (f) are zero, and the collinear component gives rise a pair of time-reversed 180° domains [$\pm l$]. Red circles and gray thick arrows in (e) represent expected shifts of pseudo-atomic positions and resulting lattice modulations with the propagation vector $\boldsymbol{k}_2$.

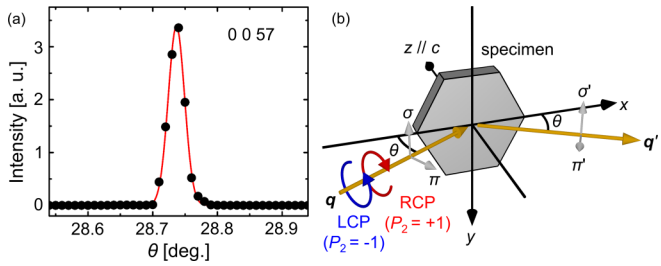

FIG. 3. (a) A rocking curve of the diffracted intensity of the (0 0 57) Bragg reflection measured by using Cu $K\alpha$ radiation. The red curve is the Gaussian fitting. (b) A schematic view of the experimental setup for the diffraction measurements. The Cartesian coordination is used to describe the magnetic form factor. The z-x plane is a scattering plane, and the z axis is parallel to the scattering vector $\hat{\boldsymbol{q}} - \widehat{\boldsymbol{q}'}$. Here θ denotes the Bragg angle, $\sigma(\sigma')$ and $\pi(\pi')$ components are perpendicular and parallel to the scattering plane, respectively. RCP and LCP represent right- and left-handed circularly polarized states, respectively.

[or 2(d)] and the out-of-plane commensurate collinear AFM component. The detail of the later component is controversial, and two different model structures have been proposed. In the first model, called as *formerly proposed* model in this paper, there is no net moment in the S block [see Fig. 2(e) or 2(f) without the blue arrows, which represent the c-axis component of the magnetic moment of the S block] [24,25]. The collinear AFM component is simple ↑↓↑↓ arrangement. On the other hand, in the second model, the S block has finite c-axis component as shown in Fig. 2(e) [or 2(f)] [21]. The collinear AFM component is ↑↑↓↓ arrangement. We call this model as *revised* model hereafter. In this paper, observed magnetic domain structures are discussed with these models.

B. Sample preparation

Single crystals of $Ba_{1.3}Sr_{0.7}CoZnFe_{11}AlO_{22}$ were grown by a flux method using Na_2O-Fe_2O_3 flux. The chemical composition of the obtained crystals was determined by the inductively coupled plasma atomic emission spectroscopy. One of the crystals was cleaved along the ab plane at an ambient condition and was used in RXD measurements. The specimen used in this study is the same as that used in Ref. [18] (thickness ≈0.5 mm) and has a fairly clean and flat face normal to the c axis. Despite the presence of some steps and cracks on the face, the flat region ($\approx 0.2 \times 0.25\,\mathrm{mm}^2$) was utilized for the domain maps shown in this paper. The full width at half maximum of the rocking curve for the (0 0 57) Bragg reflection measured by using Cu K_α radiation was ∼0.03° as shown in Fig. 3(a).

C. Resonant x-ray diffraction (RXD) measurements

The RXD measurements were performed by utilizing an ultrahigh-vacuum diffractometer at beamline 17SU, SPring-8, Japan [26]. The photon energy of incident x rays was tuned in the vicinity of Fe L_3 edge (=710 eV) by a grating apparatus. The helicity of the circularly polarized x rays was switched by electromagnets of an undulator and is described by the sign of the so-called Stokes parameter P_2. The polarization state with $P_2 = +1(-1)$ corresponds to right- (left-) handed circularly polarized x ray [27]. The incident beams were focused into ∼30 μm (∼15 μm) in a horizontal (vertical) direction by using Kirkpatrick-Baez configuration mirrors. For taking domain maps, the sample position was moved by an XYZ translation stage with 20 μm (25 μm) step in a horizontal (vertical) direction. The cleaved specimen was mounted on the diffractometer so that the c axis was in the scattering plane. The diffraction geometry is illustrated in Fig. 3(b). The experimental setup is the same with that in Ref. [17], which describes more details.

The long c-axis length (=43.44 Å) of $Ba_{1.3}Sr_{0.7}CoZnFe_{11}AlO_{22}$ is suitable for RXD study using soft x-ray with long wavelength ($\lambda = 17.45$ Å at the Fe L_3 edge) because it allows us to access the (0 0 3) Bragg reflection providing the information about the quality of the specimen within the range of the surface where the soft x-rays can penetrate. As reported in Ref. [18], the homogeneous two-dimensional intensity map of the (0 0 3) Bragg reflection confirms uniform crystallographic quality and surface state of the specimen used in this study. The penetration depth ξ of the incident beam into the specimen was estimated from the full width at half maximum ΔQ of the (0 0 3) Bragg reflection. By using the relation $\xi = 2\pi/\Delta Q$, where the unit of ΔQ is the reciprocal nanometer, the obtained penetration depth at the Fe L_3 edge is $\xi \approx 60$ nm. The ΔQ of the magnetic satellite peaks, $(0\,0\,3+\delta)$ and $(0\,0\,3+1.5)$, is comparable with that of the (0 0 3) Bragg reflection. This shows that the coherence lengths of the magnetic structure are larger than ξ.

III. GENERAL RESONANT CROSS-SECTION WITH CIRCULARLY POLARIZED X RAYS

The cross-section of RXD for magnetic materials including antiferromagnets with the incident polarized x-ray beams is generalized from that for ferromagnets [28]. Details of its derivation are given in Appendix A. We begin with the resonant dipole-transition scattering length for a single atom:

$$\begin{aligned} f_{\mathrm{atom}} = &-(\boldsymbol{\varepsilon}' \cdot \boldsymbol{\varepsilon})\left[f_0 + \left(\frac{3}{4\pi q}\right)\left(F^1_{-1} + F^1_{+1}\right)\right] \\ &- \left(\frac{3}{4\pi q}\right) i(\boldsymbol{\varepsilon}' \times \boldsymbol{\varepsilon}) \cdot \boldsymbol{m}\left(F^1_{-1} - F^1_{+1}\right) \\ &- \left(\frac{3}{4\pi q}\right)(\boldsymbol{\varepsilon}' \cdot \boldsymbol{m})(\boldsymbol{\varepsilon} \cdot \boldsymbol{m})\left(2F^1_0 - F^1_{-1} - F^1_{+1}\right) \\ &+ \boldsymbol{\varepsilon}' \cdot \boldsymbol{T} \cdot \boldsymbol{\varepsilon}, \end{aligned} \tag{1}$$

where $\boldsymbol{\varepsilon}$ and $\boldsymbol{\varepsilon}'$ are the polarization unit vectors of the incident and scattered x rays, respectively, and f_0 denotes the Thomson charge scattering. $F^1{}_\nu$, $\boldsymbol{m}$, and q are the atomic properties of the dipole transition, the unit vector directing parallel to the magnetic moment, and the wave number of the incident x rays, respectively. $\boldsymbol{T}$ in the fourth term is a tensor representing site-symmetry dependent anisotropic scattering length, i.e., the anisotropy tensor susceptibility (ATS) scattering length. We here neglect this term for simplification because polarization

dependence of ATS scattering depends on the respective case of a crystal: the space group and the index of the reflection [29,30]. The third term which is quadratic of $\boldsymbol{m}$ basically produces second-harmonic magnetic satellites. Therefore we can neglect this term as long as first-harmonic magnetic satellites are discussed except for specific conditions imposed in a magnetic structure [31]. Such particular situations are detailed in Appendix B.

The first term in Eq. (1) represents the non-magnetic charge and resonant scatterings, while the second term denotes the resonant magnetic scattering. The sum of f_{atom} with its phase for each atom located at $\boldsymbol{R}_j$ in a crystal gives the total resonant scattering length f. At the scattering vector $\boldsymbol{\tau}$ $(=\boldsymbol{q}-\boldsymbol{q}')$, where $\boldsymbol{q}$ and $\boldsymbol{q}'$ are the wave vectors of incident and scattered beams, respectively), f is written as

$$f = a(\boldsymbol{\varepsilon}' \cdot \boldsymbol{\varepsilon}) + b\boldsymbol{F}_m \cdot (\boldsymbol{\varepsilon}' \times \boldsymbol{\varepsilon}), \tag{2}$$

where $a\{=-\Sigma_j[f_0+3/(4\pi q)(F^1{}_{-1}+F^1{}_{+1})]\exp(i\boldsymbol{\tau}\cdot\boldsymbol{R}_j)\}$ is a crystal structure factor and $b[=-3/(4\pi q)i(F^1{}_{-1}-F^1{}_{+1})]$ is a coefficient. $\boldsymbol{F}_m[=\Sigma_j \boldsymbol{m}_j \exp(i\boldsymbol{\tau}\cdot\boldsymbol{R}_j)]$ is defined as a magnetic form factor [28]. Note that $\boldsymbol{F}_m$ has complex components in general because we consider arbitrary magnetic structures. By calculating the formulated polarization-dependent cross-section (See Appendix A), the circular dichroic terms in the resonant cross-section are obtained as

$$\frac{d\sigma}{d\Omega}_{\text{circ}} = -P_2\text{Im}(a^* b\boldsymbol{F}_m)\cdot(\hat{\boldsymbol{q}}+\widehat{\boldsymbol{q}'}\cos 2\theta) + P_2|b|^2\text{Im}\{[\boldsymbol{F}_m\cdot(\widehat{\boldsymbol{q}'}\times\hat{\boldsymbol{q}})](\boldsymbol{F}_m{}^*\cdot\widehat{\boldsymbol{q}'})\}. \tag{3}$$

Here, $\hat{\boldsymbol{q}}$ and $\widehat{\boldsymbol{q}'}$ are the unit vectors directing parallel to the incident and scattered beams, respectively, as shown in Fig. 3(b), and θ is the Bragg angle. The first term in Eq. (3) represents the circular dichroic charge-magnetic interference term, while the second term denotes the circular dichroic pure magnetic scattering intensity. Details of the derivation including the cases with different polarization states are described in Appendix A.

The first term in Eq. (3), i.e., the circular dichroic charge-magnetic interference term, is quite unique because it is proportional to both a and $\boldsymbol{F}_m$, which is in contrast with the second term, i.e., the magnetic scattering term with a quadratic of $\boldsymbol{F}_m$. Therefore the interference term is sensitive for the relative sign reversal of a and $\boldsymbol{F}_m$. This means that a pair of magnetic domains with the opposite sign of $\boldsymbol{F}_m$ is distinguishable when a magnetic form factor ($\boldsymbol{F}_m$) superimposes at the same reflection point with a finite crystal structure factor (a), such as on a crystallographic Bragg reflection, and the sign of a remains unchanged under the time-reversal operation. One of such pairs of domains is ferromagnetic domains [32,33], but this effect is also applicable for time-reversed 180° AFM ones [the simplest case is ↑↓↑↓ ($+l$ state) and ↓↑↓↑ ($-l$ state) collinear spin arrangements]. Therefore the interference effect can be responsible for circular dichroic RXD signals even in collinear antiferromagnets.

IV. APPLICATION TO MAGNETIC STRUCTURE OF $Ba_{1.3}Sr_{0.7}CoZnFe_{11}AlO_{22}$

A. Circular dichroic RXD and observed magnetic domain structures in $Ba_{1.3}Sr_{0.7}CoZnFe_{11}AlO_{22}$

We apply the discussion above to the observation of AFM domain structures in a magnetoelectric Y-type hexaferrite, $Ba_{1.3}Sr_{0.7}CoZnFe_{11}AlO_{22}$ [18–21]. In the previous study of resonant x-ray microdiffraction on $Ba_{1.3}Sr_{0.7}CoZnFe_{11}AlO_{22}$, circular dichroic RXD signals have been observed at both the incommensurate $(0\ 0\ 3+\delta)$ and commensurate $(0\ 0\ 3+1.5)$ reflections, which allow us to obtain spatial distributions of two pairs of AFM domains, selectively [18].

Typical domain structures obtained by the respective reflections at the same sample area are displayed in Fig. 4. Figures 4(a) and 4(b) display the two-dimensional maps of RXD intensities I_+ and I_-, respectively, at the incommensurate reflection. Here the subscript denotes the sign of P_2 in the primary beams. In Figs. 4(d) and 4(e), those at the commensurate reflection are shown. In Figs. 4(c) and 4(f), the two-dimensional maps of the flipping ratio (FR) defined as a normalized difference between RXD intensities, $(I_+ - I_-)/(I_+ + I_-)$, are plotted for $(0\ 0\ 3+\delta)$ and $(0\ 0\ 3+1.5)$, respectively. Comparing Figs. 4(c) and 4(f), we find that these

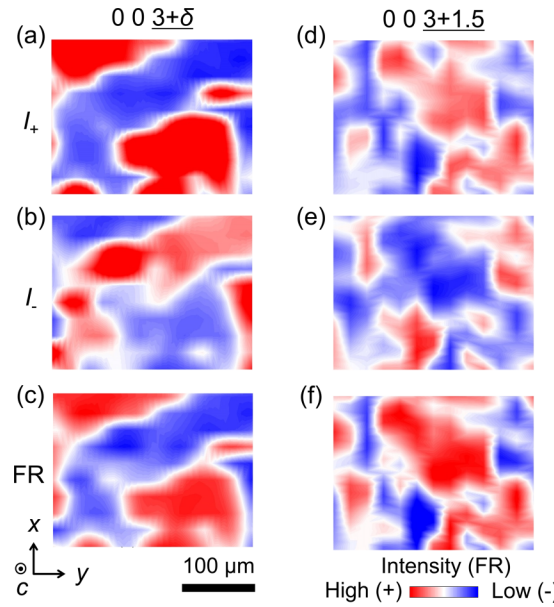

FIG. 4. Two-dimensional intensity profiles of [(a) and (b)] the incommensurate $(0\ 0\ 3+\delta)$ and [(d) and (e)] commensurate $(0\ 0\ 3+1.5)$ reflections taken at 300 K and 0 T. These measurements were carried out with x rays at 710.2 eV for $(0\ 0\ 3+\delta)$ and 709.7 eV for $(0\ 0\ 3+1.5)$ where large asymmetries in diffracted intensities between right- and left-handed incident circularly polarized beams were observed. The spatially modulated profiles in the incommensurate and commensurate reflections represent the presence of (c) helical and (f) up-up-down-down AFM domains, respectively, which are visualized by plotting the flipping ratio (FR, see text). The profiles of (a) and (d) [(b) and (e)] were obtained by right- [left-] handed circularly polarized x rays. Red and blue regions correspond to the areas where high (+) and low (−) diffracted intensity (FR) were detected.

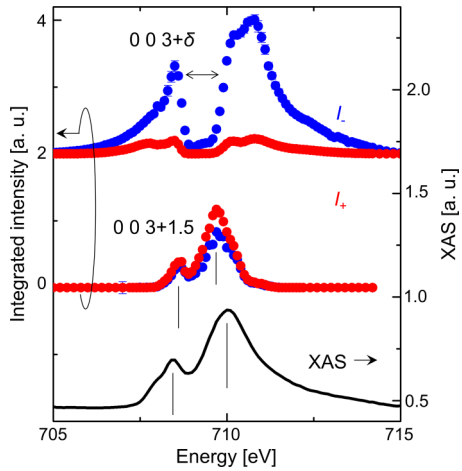

FIG. 5. Energy profiles of the integrated intensity of the incommensurate $(0\ 0\ 3+\delta)$ (top) and commensurate $(0\ 0\ 3+1.5)$ (middle) reflections measured around the Fe L_3 edge at 300 K. After subtracting fluorescence backgrounds of $2\theta/\theta$ scans measured at different photon energies, integrated intensities were obtained and plotted as functions of photon energy. The data of the incommensurate reflections are vertically shifted by 2 a.u. to enhance the visibility. Red (I_+) and blue (I_-) solid circles denote the data obtained by using right- and left-handed circularly polarized x rays, respectively. A black thick line (bottom) represents the x-ray absorption spectrum (XAS). Black thin lines and a double-headed arrow are guides to see the detailed structure of each spectrum.

two types of domain structures are obviously uncorrelated. This experimental result is consistent with that reported in Ref. [18]. The domains obtained by mapping of the circular dichroic incommensurate reflections were assigned to the helical domains (L and R) [Figs. 2(c) and 2(d)] classified into the chirality domains as in other hexaferrites [17,34]. In later sections, our discussion focuses on the origin of the magnetic domains observed by using the commensurate reflection.

The energy profile of the commensurate reflection is similar to that of the x-ray absorption spectrum (XAS) with a minor difference in the peak energies, while that of the incommensurate reflection is quite different from that of the XAS (see Fig. 5). This indicates that the energy dependent factor of the commensurate reflection is similar to that of the XAS but different from the incommensurate reflection. XAS is dominated by the attenuation coefficient which is proportional to the imaginary part of scattering length $f'' = \mathrm{Im}(F^1_{-1} + F^1_{+1})$ in antiferromagnets [28]. On the other hand, the circular dichroic term in the cross-section at the incommensurate $(0\ 0\ 3+\delta)$ reflection, which is ascribed to the well-established pure magnetic scattering [the second term in Eq. (3)], is described by

$$\frac{d\sigma}{d\Omega}^{+(-)}_{IC} \propto +(-)P_2 \cos\theta \sin 2\theta \left(F^1_{-1} - F^1_{+1}\right)^2 \qquad (4)$$

for R $(+)$ and L $(-)$ helical domains as shown in Ref. [17]. The energy dependence is dominated by the factor of $(F^1_{-1} - F^1_{+1})^2$, and shows a dip-like structure at the low energy from the main peak in the XAS as reported in Ref. [34]. The energy dependence of RXD owing to the charge-magnetic interference effect is described by the factor of $(F^1_{-1} + F^1_{+1})$ $(F^1_{-1} - F^1_{+1})$ $(\propto a^* b)$ from Eq. (3). Here we neglect nonresonant charge scatterings. The similarity of the profile of the commensurate reflection with the XAS is reasonably explained by the same energy dependent factor $(F^1_{-1} + F^1_{+1})$ with the condition that the circular dichroic RXD signal on the commensurate reflection is ascribed to the charge-magnetic interference effect. Note that lattice modulations characterized by the wave vectors $\boldsymbol{k}_1 = (0, 0, \delta)$ and $\boldsymbol{k}_2 = (0, 0, 1.5)$ are present, which was revealed by an electron diffraction measurement [18]. Therefore the crystal structure factor a is finite at $(0\ 0\ 3+1.5)$, and the interference can give rise to a circular dichroic RXD signal. The lattice modulation makes nonresonant charge scatterings nonzero at $(0\ 0\ 3+1.5)$. However, since the lattice modulations are very small, the contribution of the nonresonant charge scatterings to the reflection is far weaker than that of the resonant ones. Thus a main contribution of the $(0\ 0\ 3+1.5)$ reflection studied here is resonant scatterings.

B. Calculation of circular dichroic signals with formerly proposed magnetic structure

Here we calculate the formulated resonant cross-section obtained as Eq. (3) with the *formerly proposed* model of the ALC structure, and discuss the origin of the magnetic domains observed by mapping of the commensurate reflection. The structure consists of the in-plane helical component and the out-of-plane collinear AFM component lying only in the L blocks. The former component gives rise to a pair of helical domains [Figs. 2(c) and 2(d)], and the circular dichroic signal is ascribed to the pure magnetic scattering intensity [the second term in Eq. (3)]. The later component gives rise to a pair of time-reversed 180° AFM domains $(\pm l)$. [The lengths of each blue arrow showing the c-axis component of the S block in Figs. 2(e) and 2(f) are zero as remarked in Sec. IIA]. The formerly proposed model was adopted in the previous study [18], and the observed domains were assigned to be the time-reversed 180° AFM domains.

To calculate the circular dichroic RXD signal at $(0\ 0\ 3+1.5)$, we at first construct a magnetic structure factor $\boldsymbol{F}_m$ with the scattering vector $\boldsymbol{\tau} = (0,\ 0,\ 3+1.5)$. Since the incommensurate helical component shown in Fig. 2(c) [or 2(d)] does not contribute to the commensurate reflection, we consider only the commensurate component. Assuming that a net magnetic moment along the c axis in each block is placed at the center of each block $(z = 0,\ c/6,\ c/3,\ c/2)$ as tabulated in Table I, one finds

$$\boldsymbol{F}_m = \sum_j \boldsymbol{m}_j e^{i\boldsymbol{\tau}\cdot\boldsymbol{R}_j} = 2(0,\ 0,\ \mp i\mu_L).$$

Here, μ_L is defined by the collinear component in the L block (see the caption of Table I for explanation), and upper and lower signs correspond to a pair of the time-reversed 180° domains shown in Figs. 2(e) and 2(f) (note that net moment is zero on each S block).

The second term in Eq. (3), namely, the pure magnetic contribution, becomes zero at $(0\ 0\ 3+1.5)$ because of the orthogonal relation between $\boldsymbol{F}_m$ and $\widehat{\boldsymbol{q}'} \times \hat{\boldsymbol{q}}$. By contrast, it is possible that the charge-magnetic interference term [the

TABLE I. The magnetic moments corresponding to the commensurate components in the respective blocks of the *formerly proposed* and *revised* alternating longitudinal conical structures. The positions of the moments in the unit cell along the c axis are also shown. Here the number at each block denotes the order from the bottom side in the crystal structure shown in Fig. 2(a), and $\mu_{L(S)}$ is the sum of the unit vectors along the c axis of each magnetic moment in an L (S) block. The upper and lower signs correspond to the magnetic structures shown in Figs. 2(e) and 2(f), respectively.

	Magnetic moments in the *formerly proposed* model of ALC structure	Magnetic moments in the *revised* model of ALC structure	Positions
S1 block	$(0,\ 0,\ 0)$	$(0,\ 0,\ \mu_S)$	0
L1 block	$(0,\ 0,\ \pm\mu_L)$	$(0,\ 0,\ \pm\mu_L)$	$c/6$
S2 block	$(0,\ 0,\ 0)$	$(0,\ 0,\ -\mu_S)$	$c/3$
L2 block	$(0,\ 0,\ \mp\mu_L)$	$(0,\ 0,\ \mp\mu_L)$	$c/2$

first term in Eq. (3)] contributes to the circular-polarization dependence of the RXD signal at $(0\ 0\ 3+1.5)$ as discussed in the previous section because of the presence of a lattice modulation [18]. Such a lattice modulation makes the crystal structure factor a nonzero at $(0\ 0\ 3+1.5)$, which is necessary for the charge-magnetic interference effect to be finite. Although the strict value of a at $(0\ 0\ 3+1.5)$ is unknown so far due to the small magnitude of the distortion, we schematically illustrate one of the simplest lattice distortions with the wave vector $\boldsymbol{k}_2$ in Fig. 2(e). It is reasonably considered that the signs of a are opposite to each other for the pair of the domains shown in Figs. 2(e) and 2(f). This is because the time-reversal operation is identical with the $c/3$ translation operation which switches the directions of the local lattice distortion. Applying these conditions to Eq. (3), we obtain the circular dichroic term in Eq. (3):

$$\frac{d\sigma}{d\Omega}_{\rm circ} = -P_2 {\rm Im}[2(\pm a^*)b(\mp i\mu_L)]\hat{\boldsymbol{z}}\cdot(\hat{\boldsymbol{q}}+\widehat{\boldsymbol{q}'}\cos 2\theta)$$
$$= 2P_2\mu_L {\rm Re}(a^*b)\hat{\boldsymbol{z}}\cdot(\hat{\boldsymbol{q}}+\widehat{\boldsymbol{q}'}\cos 2\theta), \quad (5)$$

where $\hat{\boldsymbol{z}}$ is the unit vector along the c axis. Equation (5) shows that a circular dichroic signal in RXD may arise from the formerly proposed model of the ALC structure at $(0\ 0\ 3+1.5)$, but it should be homogeneous in the whole sample region because the signs of a and μ_L are coupled. Thus it is impossible to observe the time-reversed 180° domains in the ALC structure through the charge-magnetic interference effect. From the other point of view, because the time-reversal operation is identical with the $c/3$ translation operation, the difference between the time-reversed domains is in the origin choice of the unit cell. However, it is apparent that such an artificial choice does not affect the intensity calculation, and therefore we fail to identify the observed domains as the time-reversed 180° domains.

C. Calculation of circular dichroic signals with revised magnetic structure

Here, we show that the circular dichroic signals and associated magnetic domains are fully explained with the *revised* model of the ALC structure, which is recently proposed [21]. The revised model is characterized by the collinear c-axis components in both of the S and L blocks. Namely, the ALC structure consists of the in-plane helical component [Figs. 2(c) and 2(d)] and the out-of-plane collinear up-up-down-down ($\uparrow\uparrow\downarrow\downarrow$) AFM component [Figs. 2(e) and 2(f)]. The latter component alone breaks the space-inversion symmetry in the Y-type structure ($R\bar{3}m$) and induces electric polarization along c as recently reported in Ref. [21]. This means that the $\uparrow\uparrow\downarrow\downarrow$ AFM domains are simultaneously ferroelectric domains. Note that a pair of the ferroelectric $\uparrow\uparrow\downarrow\downarrow$ domains are not time-reversed 180° domains, but are transformed into each other by the space-inversion operation. Namely, the $\uparrow\uparrow\downarrow\downarrow$ AFM domains should be assigned as collinear chirality domains. Through the exchange striction mechanism [35], the $\uparrow\uparrow\downarrow\downarrow$ AFM domains can have the oppositely directed finite polarization ($\pm P$) along c. As a result, four possible magnetic domains, $[R,\ +P]$, $[L,\ +P]$, $[R,\ -P]$, and $[L,\ -P]$, will be present in the revised ALC structure.

Similar to the calculation for the formerly proposed model of the ALC structure, we here calculate the circular dichroic RXD signal for the revised model. From the net magnetic moments at the respective blocks tabulated in Table I, the magnetic form factor at the scattering vector $\boldsymbol{\tau} = (0,\ 0,\ 3+1.5)$ is assigned as

$$\boldsymbol{F}_m = \sum_j \boldsymbol{m}_j e^{i\boldsymbol{\tau}\cdot\boldsymbol{R}_j} = 2(0,\ 0,\ \mu_S \mp i\mu_L).$$

Here, μ_S is defined in the same way with μ_L. The upper and lower signs, which are defined as the relative sign reversal of the magnetic moments in the L blocks against those in the S blocks, correspond to a pair of the $\uparrow\uparrow\downarrow\downarrow$ AFM domains illustrated in Figs. 2(e) and 2(f), respectively. It is reasonably considered that the sign of a is opposite between the pair of the domains. This is because they are transformed into each other by the space-inversion operation which switches the direction of the local lattice distortion. By putting $\boldsymbol{F}_m$ into Eq. (3), the circular dichroic RXD signal is obtained as

$$\frac{d\sigma}{d\Omega}_{\rm circ} = -P_2 {\rm Im}[2(\pm a^*)b(\mu_S \mp i\mu_L)]\hat{\boldsymbol{z}}\cdot(\hat{\boldsymbol{q}}+\widehat{\boldsymbol{q}'}\cos 2\theta)$$
$$= 2P_2[\mp\mu_S {\rm Im}(a^*b)+\mu_L {\rm Re}(a^*b)]\hat{\boldsymbol{z}}\cdot(\hat{\boldsymbol{q}}+\widehat{\boldsymbol{q}'}\cos 2\theta). \quad (6)$$

Here, the upper and lower signs correspond to the domains shown in Figs. 2(e) and 2(f), respectively. Note that $\hat{\boldsymbol{q}}+\widehat{\boldsymbol{q}'}\cos 2\theta$ is not perpendicular to $\hat{\boldsymbol{z}}$ at the $(0\ 0\ 3+1.5)$ reflection, where $\theta \approx 65°$ in the Y-type hexaferrite. Equation (6) clearly indicates that the diffracted intensity at $(0\ 0\ 3+1.5)$ depends on the $\uparrow\uparrow\downarrow\downarrow$ AFM domains due to the

charge-magnetic interference term, which allows us to visualize the domain structure with the circularly polarized x-ray beams.

One may find that a circular dichroic signal also arises from the second term in the square brackets in Eq. (6) [$= \mu_L Re(a^* b)$] although this term is independent of ↑↑↓↓ AFM domains. If the contribution of this term is dominant in Eq. (6), the map of FR shown in Fig. 4(f) little reflects the ↑↑↓↓ AFM domain structure. However, the maximum and the minimum values of FR in Fig. 4(f) are +23% and −26%, respectively, and are well distinguished. This indicates that the contribution from the second term in the square brackets in Eq. (6) is much smaller than that from the first term. Thus we conclude that the FR map of the (0 0 3 + 1.5) reflection [Fig. 4(f)] is almost a direct image of the ↑↑↓↓ collinear AFM domains.

V. CONCLUSIONS

In summary, we have investigated the circular dichroic charge-magnetic interference effect in resonant x-ray diffraction from antiferromagnetic materials. The resonant magnetic scattering is interfered with not only the resonant charge scattering but also the scattering by ATS, as implied in Eq. (1) [36]. Such an interference effect also gives circular dichroic signals and can be utilized for the observation of magnetic domains, such as the time-reversed all-in-all-out magnetic domains of the pyrochlore lattice [37]. It is also possible to utilize a space-group-allowed charge scattering instead of ATS scattering. Therefore the interference effect between charge and magnetic scatterings in resonant conditions provides an opportunity for magnetic domain observation in various magnetic systems. Besides, by utilizing the ferromagnetic scattering with the propagation vector $\boldsymbol{k} = \boldsymbol{0}$, the sign reversal in a crystal structure factor, namely crystallographic antiphase domains as well as ferroelectric domains, is also detected through the interference effect in principle. This is similar to the ferroelectric domain observation by using an interference effect between the real and the imaginary parts in a crystal structure factor with resonant conditions [38].

Our finding shows that various types of AFM domains including collinear ones can be examined by utilizing the charge-magnetic interference effect, together with well-established circular dichroism on RXD emerged from the pure magnetic scattering. X-ray microscopy using dichroic resonant diffraction, combined with a light-focusing setup, can approach in an element-specific way a resolution at the scale of several tens of nanometer. It opens up a unique and innovative way for nondestructive and selective investigation of fine domain structures and their dynamics in various magnetic materials.

ACKNOWLEDGMENTS

We thank M. Taguchi and S. W. Lovesey for fruitful discussions. This work was supported by Grant-in-Aid for the JSPS Fellows (JP16J02711) and JSPS KAKENHI Grant No. JP17H01143. Resonant x-ray diffraction experiments were performed at beamline 17SU in SPring-8 with approval of RIKEN (Proposals Nos. 20160049 and 20170084).

APPENDIX A: X-RAY BRAGG DIFFRACTION IN MAGNETIC MATERIALS WITH ATOMIC RESONANCE

Here, we formulate the cross-section for the resonant x-ray diffraction (RXD) from magnetic materials (including antiferromagnets) by extending the derivation of the formula for RXD from ferromagnets [28]. First, we introduce the general resonant dipole-transition scattering length for a single atom $f_{\rm atom}$, where the polarization unit vector of the incident (scattered) x-ray beam is $\boldsymbol{\varepsilon}$ ($\boldsymbol{\varepsilon}'$),

$$\begin{aligned} f_{\rm atom} = &-(\boldsymbol{\varepsilon}'\cdot\boldsymbol{\varepsilon})\left[f_0 + \left(\frac{3}{4\pi q}\right)\left(F^1_{-1}+F^1_{+1}\right)\right] \\ &-\left(\frac{3}{4\pi q}\right) i(\boldsymbol{\varepsilon}'\times\boldsymbol{\varepsilon})\cdot\boldsymbol{m}\left(F^1_{-1}-F^1_{+1}\right) \\ &-\left(\frac{3}{4\pi q}\right)(\boldsymbol{\varepsilon}'\cdot\boldsymbol{m})(\boldsymbol{\varepsilon}\cdot\boldsymbol{m})\left(2F^1_0 - F^1_{-1} - F^1_{+1}\right) \\ &+\boldsymbol{\varepsilon}'\cdot\boldsymbol{T}\cdot\boldsymbol{\varepsilon}. \end{aligned} \tag{A1}$$

Here, f_0 denotes the Thomson charge scattering length. F^1_ν, $\boldsymbol{m}$, and q are the resonant strengths of the dipole transition with a change in magnetic quantum number ν, the unit vector being directed parallel to the magnetic moment, and the wave number of a photon, respectively. $\boldsymbol{T}$ is a tensor and represents site-symmetry dependent scattering length. Namely, the last term in Eq. (A1) is the anisotropy tensor susceptibility (ATS) scattering. However, we here neglect this term for simplification. The third term, which is quadratic in $\boldsymbol{m}$, is analogous to magnetic linear dichroism and basically produces the second-harmonic magnetic satellites. We here neglect this term for simplification, but show the calculated results with this term in Appendix B. Only in specific conditions, the quadratic term can contribute to the first-harmonic magnetic satellites [31].

The first term of Eq. (A1) represents the nonmagnetic nonresonant and resonant charge scatterings, and the second term shows the resonant magnetic scattering, which is responsible for magnetic circular dichroism in ferromagnets. The total resonant scattering factor for a crystal at the scattering vector $\boldsymbol{\tau}$ is given by

$$\begin{aligned} f = &-\sum_j e^{i\boldsymbol{\tau}\cdot\boldsymbol{R}_j}(\boldsymbol{\varepsilon}'\cdot\boldsymbol{\varepsilon})\left[f_{0j} + \left(\frac{3}{4\pi q}\right)\left(F^1_{-1}+F^1_{+1}\right)\right] \\ &-\left(\frac{3}{4\pi q}\right) i\sum_j e^{i\boldsymbol{\tau}\cdot\boldsymbol{R}_j}(\boldsymbol{\varepsilon}'\times\boldsymbol{\varepsilon})\cdot\boldsymbol{m}_j\left(F^1_{-1}-F^1_{+1}\right) \\ = &-(\boldsymbol{\varepsilon}'\cdot\boldsymbol{\varepsilon})(F_c + F'_c + iF''_c) \\ &-\left(\frac{3}{4\pi q}\right) i(\boldsymbol{\varepsilon}'\times\boldsymbol{\varepsilon})\cdot\boldsymbol{F}_m\left(F^1_{-1}-F^1_{+1}\right). \end{aligned} \tag{A2}$$

Here, $F_c[=\Sigma_j \exp(i\boldsymbol{\tau}\cdot\boldsymbol{R}_j) f_{0j}]$ and $(F'_c + iF''_c)$ $[=(3/4\pi q)$ $\Sigma_j \exp(i\boldsymbol{\tau}\cdot\boldsymbol{R}_j)(F^1_{-1}+F^1_{+1})$ are nonresonant and resonant components in a crystal structure factor, respectively. $\boldsymbol{F}_m[=\Sigma_j \exp(i\boldsymbol{\tau}\cdot\boldsymbol{R}_j)\boldsymbol{m}_j]$ is defined as a magnetic form factor [28]. $\boldsymbol{R}_j$ and $\boldsymbol{m}_j$ represent the position and the unit vector along the local magnetic moment of the atom at site j, respectively. Note that $\boldsymbol{F}_m$ has complex components in

general because we consider arbitrary magnetic structures. The photon polarization dependence is given by

$$\boldsymbol{\varepsilon}' \cdot \boldsymbol{\varepsilon} = \begin{pmatrix} \boldsymbol{\sigma}' \cdot \boldsymbol{\sigma} & \boldsymbol{\sigma}' \cdot \boldsymbol{\pi} \\ \boldsymbol{\pi}' \cdot \boldsymbol{\sigma} & \boldsymbol{\pi}' \cdot \boldsymbol{\pi} \end{pmatrix} = \begin{pmatrix} 1 & 0 \\ 0 & \hat{\boldsymbol{q}}' \cdot \hat{\boldsymbol{q}} (= \cos 2\theta) \end{pmatrix} \text{ and} \tag{A3}$$

$$\boldsymbol{\varepsilon}' \times \boldsymbol{\varepsilon} = \begin{pmatrix} \boldsymbol{\sigma}' \times \boldsymbol{\sigma} & \boldsymbol{\sigma}' \times \boldsymbol{\pi} \\ \boldsymbol{\pi}' \times \boldsymbol{\sigma} & \boldsymbol{\pi}' \times \boldsymbol{\pi} \end{pmatrix} = \begin{pmatrix} 0 & \hat{\boldsymbol{q}} \\ -\hat{\boldsymbol{q}}' & \hat{\boldsymbol{q}}' \times \hat{\boldsymbol{q}} \end{pmatrix}, \tag{A4}$$

whose bases are perpendicular ($\boldsymbol{\sigma}$ and $\boldsymbol{\sigma}'$) and parallel ($\boldsymbol{\pi}$ and $\boldsymbol{\pi}'$) to the scattering plane, where orthogonal conditions $\boldsymbol{\sigma} \times \boldsymbol{\pi} = \hat{\boldsymbol{q}}$ and $\boldsymbol{\sigma}' \times \boldsymbol{\pi}' = \hat{\boldsymbol{q}}'$ hold. Here θ is the Bragg angle, and $\hat{\boldsymbol{q}}$ ($\hat{\boldsymbol{q}}'$) is the unit vector representing the direction of the incident (scattered) beam. The scattering plane is spanned by the vectors $\hat{\boldsymbol{q}}$ and $\hat{\boldsymbol{q}}'$. The diffraction geometry is shown in Fig. 3(b).

Following the derivation given in Ref. [28], we simplify Eq. (A2) as $f = a(\boldsymbol{\varepsilon}' \cdot \boldsymbol{\varepsilon}) + b\boldsymbol{F}_m \cdot (\boldsymbol{\varepsilon}' \times \boldsymbol{\varepsilon})$ [$a = -(F_c + F_c' + iF_c'')$ and $b = -3/(4\pi q)i(F_{-1}^1 - F_{+1}^1)$]. Then f is written as

$$f = \begin{pmatrix} a & b\boldsymbol{F}_m \cdot \hat{\boldsymbol{q}} \\ -b\boldsymbol{F}_m \cdot \hat{\boldsymbol{q}}' & a\cos 2\theta + b\boldsymbol{F}_m \cdot (\hat{\boldsymbol{q}}' \times \hat{\boldsymbol{q}}) \end{pmatrix}, \tag{A5}$$

by using Eqs. (A3) and (A4). It is convenient to represent the scattering process given in Eq. (A5), by employing the unit ($\boldsymbol{I}$) and Pauli ($\boldsymbol{\sigma}$) matrices,

$$f = \boldsymbol{I}\beta + \boldsymbol{\alpha} \cdot \boldsymbol{\sigma} = \begin{pmatrix} \beta + \alpha_3 & \alpha_1 - i\alpha_2 \\ \alpha_1 + i\alpha_2 & \beta - \alpha_3 \end{pmatrix}, \tag{A6}$$

where $\boldsymbol{\alpha}[=(\alpha_1, \alpha_2, \alpha_3)]$ and β are complex number coefficients. Here, f is called the scattering amplitude operator. The expectation value of $f^\dagger f$ gives the formulated polarization-dependent cross-section $\frac{d\sigma}{d\Omega}$ by taking the trace of $\boldsymbol{\mu} f^\dagger f$ with the same bases in Eq. (A5). Namely,

$$\frac{d\sigma}{d\Omega} = \boldsymbol{\alpha}^\dagger \cdot \boldsymbol{\alpha} + \beta^*\beta + \beta^*(\boldsymbol{P} \cdot \boldsymbol{\alpha}) + (\boldsymbol{P} \cdot \boldsymbol{\alpha}^\dagger)\beta + i\boldsymbol{P} \cdot (\boldsymbol{\alpha}^\dagger \times \boldsymbol{\alpha}). \tag{A7}$$

Here, $\boldsymbol{\mu}$ is the density operator of the polarization state defined as

$$\boldsymbol{\mu} = \tfrac{1}{2}(\boldsymbol{I} + \boldsymbol{P} \cdot \boldsymbol{\sigma}),$$

where $\boldsymbol{P}[=(P_1, P_2, P_3)]$ is a vector possessing three real number parameters, the so-called Stokes parameters [28]. The polarization states with $P_1 = \pm 1$ correspond to $+45^\circ$ ($P_1 = +1$) and -45° ($P_1 = -1$) linearly polarized states, those with $P_2 = \pm 1$ correspond to right- ($P_2 = +1$) and left- ($P_2 = -1$) handed circularly polarized states, and those with $P_3 = \pm 1$ correspond to vertical ($P_3 = +1$; σ) and horizontal ($P_3 = -1$; π) linearly polarized states. The first and second terms in Eq. (A7) are independent of the polarization state described by $\boldsymbol{P}$, while the others depend on the polarization state. Comparing Eqs. (A5) and (A6), some simple algebra gives the following relations:

$$\begin{aligned} 2\beta &= a(1 + \cos 2\theta) + b\boldsymbol{F}_m \cdot (\hat{\boldsymbol{q}}' \times \hat{\boldsymbol{q}}), \\ 2\alpha_1 &= b\boldsymbol{F}_m \cdot (\hat{\boldsymbol{q}} - \hat{\boldsymbol{q}}'), \\ 2\alpha_2 &= ib\boldsymbol{F}_m \cdot (\hat{\boldsymbol{q}} + \hat{\boldsymbol{q}}'), \text{ and} \\ 2\alpha_3 &= a(1 - \cos 2\theta) - b\boldsymbol{F}_m \cdot (\hat{\boldsymbol{q}}' \times \hat{\boldsymbol{q}}). \end{aligned}$$

Using these relations, one derives the respective terms in Eq. (A7). The polarization-independent terms are

$$\boldsymbol{\alpha}^\dagger \cdot \boldsymbol{\alpha} = |\alpha_1|^2 + |\alpha_2|^2 + |\alpha_3|^2 = \tfrac{1}{4}[2|b|^2(|\boldsymbol{F}_m \cdot \hat{\boldsymbol{q}}|^2 + |\boldsymbol{F}_m \cdot \hat{\boldsymbol{q}}'|^2) + |a|^2(1 - \cos 2\theta)^2 - (a^*b\boldsymbol{F}_m + ab^*\boldsymbol{F}_m{}^*) \cdot (\hat{\boldsymbol{q}}' \times \hat{\boldsymbol{q}})(1 - \cos 2\theta) + |b|^2|\boldsymbol{F}_m \cdot (\hat{\boldsymbol{q}}' \times \hat{\boldsymbol{q}})|^2] \quad \text{and} \tag{A8}$$

$$\beta^*\beta = \tfrac{1}{4}[|a|^2(1 + \cos 2\theta)^2 + (a^*b\boldsymbol{F}_m + ab^*\boldsymbol{F}_m{}^*) \cdot (\hat{\boldsymbol{q}}' \times \hat{\boldsymbol{q}})(1 + \cos 2\theta) + |b|^2|\boldsymbol{F}_m \cdot (\hat{\boldsymbol{q}}' \times \hat{\boldsymbol{q}})|^2]. \tag{A9}$$

Then the polarization-independent terms of the resonant cross-section are

$$\begin{aligned} \frac{d\sigma}{d\Omega}_0 &= \frac{|a|^2}{2}(1 + \cos^2 2\theta) + \frac{1}{2}(a^*b\boldsymbol{F}_m + ab^*\boldsymbol{F}_m{}^*) \cdot (\hat{\boldsymbol{q}}' \times \hat{\boldsymbol{q}}) \cos 2\theta + \frac{|b|^2}{2}(|\boldsymbol{F}_m \cdot \hat{\boldsymbol{q}}|^2 + |\boldsymbol{F}_m \cdot (\hat{\boldsymbol{q}}' \times \hat{\boldsymbol{q}})|^2 + |\boldsymbol{F}_m \cdot \hat{\boldsymbol{q}}'|^2) \\ &= \frac{|a|^2}{2}(1 + \cos^2 2\theta) + \cos 2\theta \mathrm{Re}(a^*b\boldsymbol{F}_m) \cdot (\hat{\boldsymbol{q}}' \times \hat{\boldsymbol{q}}) + \frac{|b|^2}{2}(|\boldsymbol{F}_m \cdot \hat{\boldsymbol{q}}|^2 + |\boldsymbol{F}_m \cdot (\hat{\boldsymbol{q}}' \times \hat{\boldsymbol{q}})|^2 + |\boldsymbol{F}_m \cdot \hat{\boldsymbol{q}}'|^2). \end{aligned} \tag{A10}$$

The first term is the pure charge scattering intensity including both resonant and nonresonant charge scatterings, the second term is the charge-magnetic interference term, and the last term is the pure magnetic scattering intensity.

Next, the polarization-dependent terms of the resonant cross-section are discussed with three polarization states: $\boldsymbol{P} = (P_1, 0, 0)$, $(0, P_2, 0)$, and $(0, 0, P_3)$.

The case of $\boldsymbol{P} = (P_1, 0, 0)$. The polarization-dependent terms in Eq. (A7) for the polarization state $\boldsymbol{P} = (P_1, 0, 0)$ are

$$\beta^*(\boldsymbol{P} \cdot \boldsymbol{\alpha}) = \tfrac{1}{4}P_1\{(1 + \cos 2\theta)a^*b\boldsymbol{F}_m \cdot (\hat{\boldsymbol{q}} - \hat{\boldsymbol{q}}') + |b|^2[\boldsymbol{F}_m{}^* \cdot (\hat{\boldsymbol{q}}' \times \hat{\boldsymbol{q}})][\boldsymbol{F}_m \cdot (\hat{\boldsymbol{q}} - \hat{\boldsymbol{q}}')]\}, \tag{A11}$$

$$(\boldsymbol{P} \cdot \boldsymbol{\alpha}^\dagger)\beta = \tfrac{1}{4}P_1\{(1 + \cos 2\theta)ab^*\boldsymbol{F}_m{}^* \cdot (\hat{\boldsymbol{q}} - \hat{\boldsymbol{q}}') + |b|^2[\boldsymbol{F}_m \cdot (\hat{\boldsymbol{q}}' \times \hat{\boldsymbol{q}})][\boldsymbol{F}_m{}^* \cdot (\hat{\boldsymbol{q}} - \hat{\boldsymbol{q}}')]\}, \text{ and} \tag{A12}$$

$$i\boldsymbol{P}\cdot(\boldsymbol{\alpha}^{\dagger}\times\boldsymbol{\alpha}) = \tfrac{1}{4}P_1((1-\cos 2\theta)(a^*b\boldsymbol{F}_m + ab^*\boldsymbol{F}_m{}^*)\cdot(\hat{\boldsymbol{q}}+\widehat{\boldsymbol{q}'}) - |b|^2\{[\boldsymbol{F}_m{}^*\cdot(\widehat{\boldsymbol{q}'}\times\hat{\boldsymbol{q}})][\boldsymbol{F}_m\cdot(\hat{\boldsymbol{q}}+\widehat{\boldsymbol{q}'})] + [\boldsymbol{F}_m\cdot(\widehat{\boldsymbol{q}'}\times\hat{\boldsymbol{q}})] + [\boldsymbol{F}_m{}^*\cdot(\hat{\boldsymbol{q}}+\widehat{\boldsymbol{q}'})]\}), \tag{A13}$$

respectively. Summing up Eqs. (A11)–(A13), one obtains the linear dichroic (for the $\pm 45^\circ$ polarization states) terms in the resonant cross-section:

$$\frac{d\sigma}{d\Omega}_{P_1} = \frac{1}{2}P_1(a^*b\boldsymbol{F}_m + ab^*\boldsymbol{F}_m{}^*)\cdot(\hat{\boldsymbol{q}}-\widehat{\boldsymbol{q}'}\cos 2\theta) - \frac{|b|^2}{2}P_1\{[\boldsymbol{F}_m\cdot(\widehat{\boldsymbol{q}'}\times\hat{\boldsymbol{q}})](\boldsymbol{F}_m{}^*\cdot\widehat{\boldsymbol{q}'}) + [\boldsymbol{F}_m{}^*\cdot(\widehat{\boldsymbol{q}'}\times\hat{\boldsymbol{q}})](\boldsymbol{F}_m\cdot\widehat{\boldsymbol{q}'})\}$$
$$= P_1\mathrm{Re}(a^*b\boldsymbol{F}_m)\cdot(\hat{\boldsymbol{q}}-\widehat{\boldsymbol{q}'}\cos 2\theta) - P_1|b|^2\mathrm{Re}\{[\boldsymbol{F}_m\cdot(\widehat{\boldsymbol{q}'}\times\hat{\boldsymbol{q}})](\boldsymbol{F}_m{}^*\cdot\widehat{\boldsymbol{q}'})\}. \tag{A14}$$

The first term shows the linear dichroic charge-magnetic interference term, while the second term is the linear dichroic pure magnetic scattering intensity.

The case of $\boldsymbol{P} = (0,\ P_2,\ 0)$. The polarization-dependent terms in Eq. (A7) for the polarization state $\boldsymbol{P} = (0, P_2, 0)$ are

$$\beta^*(\boldsymbol{P}\cdot\boldsymbol{\alpha}) = \tfrac{1}{4}P_2\{(1+\cos 2\theta)a^*b\boldsymbol{F}_m\cdot(\hat{\boldsymbol{q}}+\widehat{\boldsymbol{q}'}) + |b|^2[\boldsymbol{F}_m{}^*\cdot(\widehat{\boldsymbol{q}'}\times\hat{\boldsymbol{q}})][\boldsymbol{F}_m\cdot(\hat{\boldsymbol{q}}+\widehat{\boldsymbol{q}'})]\}, \tag{A15}$$

$$(\boldsymbol{P}\cdot\boldsymbol{\alpha}^{\dagger})\beta = \tfrac{1}{4}P_2\{(1+\cos 2\theta)ab^*\boldsymbol{F}_m{}^*\cdot(\hat{\boldsymbol{q}}+\widehat{\boldsymbol{q}'}) + |b|^2[\boldsymbol{F}_m\cdot(\widehat{\boldsymbol{q}'}\times\hat{\boldsymbol{q}})][\boldsymbol{F}_m{}^*\cdot(\hat{\boldsymbol{q}}+\widehat{\boldsymbol{q}'})]\},\ \text{and} \tag{A16}$$

$$i\boldsymbol{P}\cdot(\boldsymbol{\alpha}^{\dagger}\times\boldsymbol{\alpha}) = \tfrac{1}{4}P_2((1-\cos 2\theta)(a^*b\boldsymbol{F}_m - ab^*\boldsymbol{F}_m{}^*)\cdot(\hat{\boldsymbol{q}}-\widehat{\boldsymbol{q}'}) - |b|^2\{[\boldsymbol{F}_m{}^*\cdot(\widehat{\boldsymbol{q}'}\times\hat{\boldsymbol{q}})][\boldsymbol{F}_m\cdot(\hat{\boldsymbol{q}}-\widehat{\boldsymbol{q}'})] + [\boldsymbol{F}_m\cdot(\widehat{\boldsymbol{q}'}\times\hat{\boldsymbol{q}})][\boldsymbol{F}_m{}^*\cdot(\hat{\boldsymbol{q}}-\widehat{\boldsymbol{q}'})]\}), \tag{A17}$$

respectively. Summing up Eqs. (A15)–(A17), one obtains the circular dichroic terms in resonant cross-section:

$$\frac{d\sigma}{d\Omega}_{\mathrm{circ}} = \frac{i}{2}P_2(a^*b\boldsymbol{F}_m - ab^*\boldsymbol{F}_m{}^*)\cdot(\hat{\boldsymbol{q}}+\widehat{\boldsymbol{q}'}\cos 2\theta) + \frac{i|b|^2}{2}P_2\{-[\boldsymbol{F}_m\cdot(\widehat{\boldsymbol{q}'}\times\hat{\boldsymbol{q}})](\boldsymbol{F}_m{}^*\cdot\widehat{\boldsymbol{q}'}) + [\boldsymbol{F}_m{}^*\cdot(\widehat{\boldsymbol{q}'}\times\hat{\boldsymbol{q}})](\boldsymbol{F}_m\cdot\widehat{\boldsymbol{q}'})\}$$
$$= -P_2\mathrm{Im}(a^*b\boldsymbol{F}_m)\cdot(\hat{\boldsymbol{q}}+\widehat{\boldsymbol{q}'}\cos 2\theta) + P_2|b|^2\mathrm{Im}\{[\boldsymbol{F}_m\cdot(\widehat{\boldsymbol{q}'}\times\hat{\boldsymbol{q}})](\boldsymbol{F}_m{}^*\cdot\widehat{\boldsymbol{q}'})\}. \tag{A18}$$

The first term is the circular dichroic charge-magnetic interference term, while the second term is the circular dichroic pure magnetic scattering intensity. The second term provides the polarization-dependent scattering in spiral magnets [15–17]. It is notable that the circular dichroic charge-magnetic interference term is proportional to both of the first order of a and $\boldsymbol{F}_m$, not to their quadratics, unlike in the pure magnetic scattering intensity with the quadratic of $\boldsymbol{F}_m$. Therefore the first term is sensitive for the relative sign reversal of a and $\boldsymbol{F}_m$. This means that pairs of magnetic domains with opposite sign of $\boldsymbol{F}_m$ can be distinguished if the interference term is finite and the sign of a is unchanged.

The case of $\boldsymbol{P} = (0, 0, P_3)$. The polarization-dependent terms in Eq. (A7) for the polarization state with $\boldsymbol{P} = (0, 0, P_3)$ are

$$\beta^*(\boldsymbol{P}\cdot\boldsymbol{\alpha}) = \frac{1}{4}P_3\{|a|^2\sin^2 2\theta - (a^*b\boldsymbol{F}_m - ab^*\boldsymbol{F}_m{}^*)\cdot(\widehat{\boldsymbol{q}'}\times\hat{\boldsymbol{q}}) - \cos 2\theta(a^*b\boldsymbol{F}_m + ab^*\boldsymbol{F}_m{}^*)$$
$$\cdot(\widehat{\boldsymbol{q}'}\times\hat{\boldsymbol{q}}) - |b|^2|\boldsymbol{F}_m\cdot(\widehat{\boldsymbol{q}'}\times\hat{\boldsymbol{q}})|^2\}, \tag{A19}$$

$$(\boldsymbol{P}\cdot\boldsymbol{\alpha}^{\dagger})\beta = \frac{1}{4}P_3\{|a|^2\sin^2 2\theta + (a^*b\boldsymbol{F}_m - ab^*\boldsymbol{F}_m{}^*)\cdot(\widehat{\boldsymbol{q}'}\times\hat{\boldsymbol{q}}) - \cos 2\theta(a^*b\boldsymbol{F}_m + ab^*\boldsymbol{F}_m{}^*)$$
$$\cdot(\widehat{\boldsymbol{q}'}\times\hat{\boldsymbol{q}}) - |b|^2|\boldsymbol{F}_m\cdot(\widehat{\boldsymbol{q}'}\times\hat{\boldsymbol{q}})|^2\},\ \text{and} \tag{A20}$$

$$i\boldsymbol{P}\cdot(\boldsymbol{\alpha}^{\dagger}\times\boldsymbol{\alpha}) = -\frac{|b|^2}{4}P_3\{[\boldsymbol{F}_m{}^*\cdot(\hat{\boldsymbol{q}}-\widehat{\boldsymbol{q}'})][\boldsymbol{F}_m\cdot(\hat{\boldsymbol{q}}+\widehat{\boldsymbol{q}'})] + [\boldsymbol{F}_m\cdot(\hat{\boldsymbol{q}}-\widehat{\boldsymbol{q}'})][\boldsymbol{F}_m{}^*\cdot(\hat{\boldsymbol{q}}+\widehat{\boldsymbol{q}'})]\}, \tag{A21}$$

respectively. Summing up Eqs. (A19)–(A21), one obtains the linear dichroic terms for the σ and π polarization states in the resonant cross-section:

$$\frac{d\sigma}{d\Omega}_{P_3} = P_3\frac{|a|^2}{2}\sin^2 2\theta - \frac{1}{2}P_3\cos 2\theta(a^*b\boldsymbol{F}_m + ab^*\boldsymbol{F}_m{}^*)\cdot(\widehat{\boldsymbol{q}'}\times\hat{\boldsymbol{q}})$$
$$- P_3\frac{|b|^2}{4}\{[\boldsymbol{F}_m{}^*\cdot(\hat{\boldsymbol{q}}-\widehat{\boldsymbol{q}'})][\boldsymbol{F}_m\cdot(\hat{\boldsymbol{q}}+\widehat{\boldsymbol{q}'})] + 2|\boldsymbol{F}_m\cdot(\widehat{\boldsymbol{q}'}\times\hat{\boldsymbol{q}})|^2 + [\boldsymbol{F}_m\cdot(\hat{\boldsymbol{q}}-\widehat{\boldsymbol{q}'})][\boldsymbol{F}_m{}^*\cdot(\hat{\boldsymbol{q}}+\widehat{\boldsymbol{q}'})]\}$$
$$= P_3\frac{|a|^2}{2}\sin^2 2\theta - P_3\cos 2\theta\mathrm{Re}(a^*b\boldsymbol{F}_m)\cdot(\widehat{\boldsymbol{q}'}\times\hat{\boldsymbol{q}}) - P_3\frac{|b|^2}{2}(|\boldsymbol{F}_m\cdot\hat{\boldsymbol{q}}|^2 + |\boldsymbol{F}_m\cdot(\widehat{\boldsymbol{q}'}\times\hat{\boldsymbol{q}})|^2 - |\boldsymbol{F}_m\cdot\widehat{\boldsymbol{q}'}|^2). \tag{A22}$$

The first term shows the linear dichroic pure charge scattering intensity by both resonant and nonresonant scatterings. The second term represents the linear dichroic charge-magnetic interference term, while the last term is the linear dichroic pure magnetic scattering intensity.

APPENDIX B: CALCULATION OF RESONANT CROSS-SECTION WITH A QUADRATIC TERM OF MAGNETIC MOMENT

Here we show the calculated results of resonant cross-section taking into account the quadratic term of $\boldsymbol{m}$ ($f^{(2)}_{\rm atom}$) in the general resonant dipole-transition scattering length for a single atom. The polarization dependence of the term is described as

$$f^{(2)}_{\rm atom} = -\left(\frac{3}{4\pi q}\right)(\boldsymbol{\varepsilon}'\cdot\boldsymbol{m})(\boldsymbol{\varepsilon}\cdot\boldsymbol{m})\left(2F^1_0 - F^1_{-1} - F^1_{+1}\right) = -\left(\frac{3}{4\pi q}\right)\left(2F^1_0 - F^1_{-1} - F_{+1^1}\right) \times \begin{pmatrix} m_y^2 & -m_y(m_x\sin\theta - m_z\cos\theta) \\ m_y(m_x\sin\theta + m_z\cos\theta) & -m_x^2\sin^2\theta - m_z^2\cos^2\theta \end{pmatrix}, \tag{A23}$$

where m_x, m_y, and m_z denote the components of $\boldsymbol{m}$ along the axes shown in Fig. 3(b) [31]. The sum of the term with its phase for each atom located at $\boldsymbol{R}_j$ in a crystal gives the contribution of the term to the total resonant scattering length $f^{(2)}$ at the scattering vector $\boldsymbol{\tau}$:

$$f^{(2)} = -\left(\frac{3}{4\pi q}\right)\left(2F^1_0 - F^1_{-1} - F^1_{+1}\right) \times \sum_j \begin{pmatrix} m_{yj}^2 e^{i\boldsymbol{\tau}\cdot\boldsymbol{R}_j} & -m_{xj}m_{yj}e^{i\boldsymbol{\tau}\cdot\boldsymbol{R}_j}\sin\theta + m_{yj}m_{zj}e^{i\boldsymbol{\tau}\cdot\boldsymbol{R}_j}\cos\theta \\ m_{xj}m_{yj}e^{i\boldsymbol{\tau}\cdot\boldsymbol{R}_j}\sin\theta + m_{yj}m_{zj}e^{i\boldsymbol{\tau}\cdot\boldsymbol{R}_j}\cos\theta & -m_{xj}^2e^{i\boldsymbol{\tau}\cdot\boldsymbol{R}_j}\sin^2\theta - m_{zj}^2e^{i\boldsymbol{\tau}\cdot\boldsymbol{R}_j}\cos^2\theta \end{pmatrix}.$$

By representing each summation that appears in the above formula as $\Sigma_j m_{sj}m_{tj}\exp(i\boldsymbol{\tau}\cdot\boldsymbol{R}_j) = M_{st}$, where $s, t = x, y, z$ and $c = -(3/4\pi q)(2F^1_0 - F^1_{-1} - F^1_{+1})$, $f^{(2)}$ is simplified as

$$f^{(2)} = c\begin{pmatrix} M_{yy} & -M_{xy}\sin\theta + M_{yz}\cos\theta \\ M_{xy}\sin\theta + M_{yz}\cos\theta & -M_{xx}\sin^2\theta - M_{zz}\cos^2\theta \end{pmatrix}. \tag{A24}$$

By adding the charge scattering term and the magnetic scattering term, which is linear in $\boldsymbol{m}$, the total resonant scattering length is obtained as

$$f = \begin{pmatrix} a + cM_{yy} & b\boldsymbol{F}_m\cdot\hat{\boldsymbol{q}} + c(-M_{xy}\sin\theta + M_{yz}\cos\theta) \\ -b\boldsymbol{F}_m\cdot\widehat{\boldsymbol{q}'} + c(M_{xy}\sin\theta + M_{yz}\cos\theta) & a\cos 2\theta + b\boldsymbol{F}_m\cdot(\widehat{\boldsymbol{q}'}\times\hat{\boldsymbol{q}}) - c(M_{xx}\sin^2\theta + M_{zz}\cos^2\theta) \end{pmatrix}. \tag{A25}$$

The same calculation procedure with Appendix A provides the resonant cross-section, as follows. The polarization-independent terms are

$$\begin{aligned} \frac{d\sigma}{d\Omega}_0 &= \frac{|a|^2}{2}(1+\cos^2 2\theta) + \cos 2\theta\,\mathrm{Re}(a^*b\boldsymbol{F}_m)\cdot(\widehat{\boldsymbol{q}'}\times\hat{\boldsymbol{q}}) + \frac{|b|^2}{2}(|\boldsymbol{F}_m\cdot\hat{\boldsymbol{q}}|^2 + |\boldsymbol{F}_m\cdot(\widehat{\boldsymbol{q}'}\times\hat{\boldsymbol{q}})|^2 + |\boldsymbol{F}_m\cdot\widehat{\boldsymbol{q}'}|^2) \\ &+ \frac{|c|^2}{2}[|M_{yy}|^2 + |M_{xx}\sin^2\theta + M_{zz}\cos^2\theta|^2 + 2(|M_{xy}|^2\sin^2\theta + |M_{yz}|^2\cos^2\theta)] \\ &+ \mathrm{Re}\{a^*c[M_{yy} - (|M_{xx}|^2\sin^2\theta + |M_{zz}|^2\cos^2\theta)\cos 2\theta]\} \\ &+ \mathrm{Re}\{b^*c[\boldsymbol{F}_m{}^*\cdot(\hat{\boldsymbol{q}} - \widehat{\boldsymbol{q}'})M_{yz}\cos\theta - \boldsymbol{F}_m{}^*\cdot(\hat{\boldsymbol{q}} + \widehat{\boldsymbol{q}'})M_{xy}\sin\theta - \boldsymbol{F}_m{}^*\cdot(\widehat{\boldsymbol{q}'}\times\hat{\boldsymbol{q}})(M_{xx}\sin^2\theta + M_{zz}\cos^2\theta)]\}. \end{aligned} \tag{A26}$$

The linear dichroic (for the $\pm 45^\circ$ polarization states) terms are

$$\begin{aligned} \frac{d\sigma}{d\Omega}_{P_1} &= P_1\mathrm{Re}(a^*b\boldsymbol{F}_m)\cdot(\hat{\boldsymbol{q}} - \widehat{\boldsymbol{q}'}\cos 2\theta) - P_1|b|^2\mathrm{Re}\{[\boldsymbol{F}_m\cdot(\widehat{\boldsymbol{q}'}\times\hat{\boldsymbol{q}})](\boldsymbol{F}_m{}^*\cdot\widehat{\boldsymbol{q}'})\} \\ &+ P_1|c|^2\mathrm{Re}[M_{yy}{}^*(M_{yz}\cos\theta - M_{xy}\sin\theta) - (M_{xx}{}^*\sin^2\theta + M_{zz}{}^*\cos^2\theta)(M_{yz}\cos\theta + M_{xy}\sin\theta)] \\ &+ 2P_1\mathrm{Re}[a^*c(M_{yz}\cos^3\theta - M_{xy}\sin^3\theta)] \\ &+ P_1\mathrm{Re}\{b^*c[\boldsymbol{F}_m{}^*\cdot(\widehat{\boldsymbol{q}'}\times\hat{\boldsymbol{q}})(M_{yz}\cos\theta + M_{xy}\sin\theta) + \boldsymbol{F}_m{}^*\cdot\hat{\boldsymbol{q}}M_{yy} + \boldsymbol{F}_m{}^*\cdot\widehat{\boldsymbol{q}'}(M_{xx}\sin^2\theta + M_{zz}\cos^2\theta)]\}. \end{aligned} \tag{A27}$$

The circular dichroic terms are

$$\begin{aligned} \frac{d\sigma}{d\Omega}_{\rm circ} &= -P_2\mathrm{Im}(a^*b\boldsymbol{F}_m)\cdot(\hat{\boldsymbol{q}} + \widehat{\boldsymbol{q}'}\cos 2\theta) + P_2|b|^2\mathrm{Im}\{[\boldsymbol{F}_m\cdot(\widehat{\boldsymbol{q}'}\times\hat{\boldsymbol{q}})](\boldsymbol{F}_m{}^*\cdot\widehat{\boldsymbol{q}'})\} \\ &- P_2|c|^2\mathrm{Im}[M_{yy}{}^*(M_{xy}\sin\theta + M_{yz}\cos\theta) - (M_{xx}{}^*\sin^2\theta + M_{zz}{}^*\cos^2\theta)(M_{xy}\sin\theta - M_{yz}\cos\theta)] \\ &+ P_2\sin 2\theta\,\mathrm{Im}[a^*c(M_{xy}\cos\theta - M_{yz}\sin\theta)] \\ &+ P_2\mathrm{Im}\{b^*c[\boldsymbol{F}_m{}^*\cdot(\widehat{\boldsymbol{q}'}\times\hat{\boldsymbol{q}})(M_{yz}\sin\theta + M_{yz}\cos\theta) + \boldsymbol{F}_m{}^*\cdot\hat{\boldsymbol{q}}M_{yy} - \boldsymbol{F}_m{}^*\cdot\widehat{\boldsymbol{q}'}(M_{xx}\sin^2\theta + M_{zz}\cos^2\theta)]\}. \end{aligned} \tag{A28}$$

The linear dichroic terms for the σ and π polarization states:

$$\begin{aligned}\frac{d\sigma}{d\Omega}_{P_3} &= P_3\frac{|a|^2}{2}\sin^2 2\theta - P_3\cos 2\theta \mathrm{Re}(a^* b\boldsymbol{F}_m)\cdot(\widehat{\boldsymbol{q}'}\times\hat{\boldsymbol{q}}) - P_3\frac{|b|^2}{2}(|\boldsymbol{F}_m\cdot\hat{\boldsymbol{q}}|^2 + |\boldsymbol{F}_m\cdot(\widehat{\boldsymbol{q}'}\times\hat{\boldsymbol{q}})|^2 - |\boldsymbol{F}_m\cdot\widehat{\boldsymbol{q}'}|^2)\\ &+ P_3\frac{|c|^2}{2}[|M_{yy}|^2 - |M_{xx}\sin^2\theta + M_{zz}\cos^2\theta|^2 + 2\sin 2\theta\mathrm{Re}(M_{xy}M_{yz}{}^*)]\\ &+ P_3\mathrm{Re}\{a^* c[M_{yy} + (M_{xx}\sin^2\theta + M_{zz}\cos^2\theta)\cos 2\theta]\}\\ &+ P_3\mathrm{Re}\{b^* c[\boldsymbol{F}_m{}^*\cdot(\widehat{\boldsymbol{q}'}\times\hat{\boldsymbol{q}})(M_{xx}{}^*\sin^2\theta + M_{zz}{}^*\cos^2\theta) + \boldsymbol{F}_m{}^*\cdot(\hat{\boldsymbol{q}} - \widehat{\boldsymbol{q}'})M_{xy}\sin\theta - \boldsymbol{F}_m{}^*\cdot(\hat{\boldsymbol{q}} + \widehat{\boldsymbol{q}'})M_{yz}\cos\theta]\}.\end{aligned} \tag{A29}$$

In Eqs. (A26)–(A29), the terms that are proportional to $|a|^2$, $|b|^2$, and $|c|^2$ represent pure charge scattering, pure magnetic scattering from the linear term of $\boldsymbol{m}$, and that from the quadratic term of $\boldsymbol{m}$, respectively. The cross coupling terms which are proportional to a^*b, a^*c, and b^*c show interference terms between charge and magnetic (linear term of $\boldsymbol{m}$) scatterings, charge and magnetic (quadratic of $\boldsymbol{m}$) scatterings, and magnetic (linear to $\boldsymbol{m}$) and magnetic (quadratic of $\boldsymbol{m}$) scatterings, respectively.

Let us consider the contribution of the magnetic scattering term with a quadratic $\boldsymbol{m}$. In a magnetic material with a single modulation vector $\boldsymbol{k}$, the magnetic moment at the site j, $\boldsymbol{m}_j$, can be described by using $\exp(i\boldsymbol{k}\cdot\boldsymbol{R}_j)$ and $\exp(-i\boldsymbol{k}\cdot\boldsymbol{R}_j)$. Then, each component that appears in Eq. (A23) is written with the phase factors of $\exp(2i\boldsymbol{k}\cdot\boldsymbol{R}_j)$, $\exp(-2i\boldsymbol{k}\cdot\boldsymbol{R}_j)$, and $\exp[i(\boldsymbol{k}-\boldsymbol{k})\cdot\boldsymbol{R}_j]$ $(=1)$. The former two factors produce second-harmonic magnetic satellites, while the last one contributes to the fundamental reflection. Thus, as long as first-order magnetic satellites are considered in magnetic structures described by a single modulation vector, the magnetic scattering term that is proportional to square of $\boldsymbol{m}$ can be neglected even in terms of dichroism in RXD.

However, depending on magnetic structures, the term can contribute to the first-order magnetic satellites and provide dichroic signals on the reflections. Such a magnetic structure has a ferromagnetic component ($\boldsymbol{k}=\boldsymbol{0}$) in addition to a modulated structure ($\boldsymbol{k}\neq\boldsymbol{0}$) such as a spiral structure. One of such specific magnetic structures is the so-called normal longitudinal conical structure reported in rare-earth metals [39,40] and several types of hexaferrites [22]. When the modulation vector with nonzero component $\boldsymbol{k}$ in the normal longitudinal conical structure is parallel to the scattering vector $\boldsymbol{\tau}$, m_x and m_y are spatially modulated along $\boldsymbol{k}$ with the phase factors of $\exp(i\boldsymbol{k}\cdot\boldsymbol{R}_j)$ and $\exp(-i\boldsymbol{k}\cdot\boldsymbol{R}_j)$. On the other hand, m_z is represented by a zero wave vector and has nonzero constant. In this case, the linear component of m_z in Eq. (A23), $M_{yz}[=\Sigma_j m_{yj}m_{zj}\exp(i\boldsymbol{\tau}\cdot\boldsymbol{R}_j)]$, is finite at the first-order magnetic satellites. This component appears in all of the formulated cross-sections obtained as Eqs. (A26)–(A29).

[1] J. Nogués and I. K. Schuller, Exchange bias, J. Mag. Mag. Mater. **192**, 203 (1999).

[2] M. Fiebig, Revival of the magnetoelectric effect, J. Phys. D **38**, R123 (2005).

[3] P. J. Brown, Magnetic structure studied with zero-field polarimetry, Physica B **192**, 14 (1993).

[4] M. Fiebig, D. Fröhlich, St. Leute, and R. V. Pisarev, Topography of antiferromagnetic domains using second harmonic generation with an external reference, Appl. Phys. B **66**, 265 (1998).

[5] P. J. Brown, *Neutron Scattering from Magnetic Materials* (Elsevier, New York, 2005), pp. 215–244.

[6] F. U. Hillebrecht, H. Ohldag, N. B. Weber, C. Bethke, U. Mick, M. Weiss, and J. Bahrdt, Magnetic Moments at the Surface of Antiferromagnetic NiO(100), Phys. Rev. Lett. **86**, 3419 (2001).

[7] H. Ohldag, A. Scholl, F. Nolting, S. Anders, F. U. Hillebrecht, and A. Stöhr, Spin Reorientation at the Antiferromagnetic NiO(001) Surface in Response to an Adjacent Ferromagnet, Phys. Rev. Lett. **86**, 2878 (2001).

[8] J. Baruchel and M. Schlenker, Observation of antiferromagnetic domains in nickel oxide by neutron diffraction topography, J. Appl. Phys. **48**, 5 (1977).

[9] H. Ohldag, T. J. Regan, J. Stöhr, A. Scholl, F. Nolting, J. Lüning, C. Stamm, S. Anders, and R. L. White, Spectroscopic Identification and Direct Imaging of Interfacial Magnetic Spins, Phys. Rev. Lett. **87**, 247201 (2001).

[10] J. Baruchel, M. Schlenker, and B. Barbara, 180° antiferromagnetic domains in MnF_2 by neutron topography, J. Mag. Mag. Mater. **15–18**, 1510 (1980).

[11] J. Baruchel, X-ray and neutron topographical studies of magnetic materials, Physica B **192**, 79 (1993).

[12] M. Fiebig, D. Fröhlich, G. v L. Sluyterman, and R. V. Pisarev, Domain topography of antiferromagnetic Cr_2O_3 by second-harmonic generation, Appl. Phys. Lett. **66**, 2906 (1995).

[13] J. Baruchel, G. Aubert, S. B. Palmer, and M. Schlenker, Observation of Ferro-helimagnetic phase coexistence in Tb crystals, J. Magn. Magn. Mater. **54–57**, 1631 (1986).

[14] M. Matsubara, S. Manz, M. Mochizuki, T. Kubacka, A. Iyama, N. Aliouane, T. Kimura, S. L. Johnson, D. Meier, and M. Fiebig, Magnetoelectric domain control in multiferroic $TbMnO_3$, Science **348**, 1112 (2015).

[15] J. C. Lang, D. R. Lee, D. Haskel, and G. Srajer, Imaging spiral magnetic domains in Ho metal using circularly polarized Bragg diffraction, J. Appl. Phys. **95**, 6537 (2004).

[16] E. Schierle, V. Soltwisch, D. Schmitz, R. Feyerherm, A. Maljuk, F. Yokaichiya, D. N. Argyriou, and E. Weschke, Cycloidal Order of 4f Moments as a Probe of Chiral Domains in $DyMnO_3$, Phys. Rev. Lett. **105**, 167207 (2010).

[17] Y. Hiraoka, Y. Tanaka, T. Kojima, Y. Takata, M. Oura, Y. Senba, H. Ohashi, Y. Wakabayashi, S. Shin, and T. Kimura, Spin-chiral domains in $Ba_{0.5}Sr_{1.5}Zn_2Fe_{12}O_{22}$ observed by scanning resonant x-ray microdiffraction, Phys. Rev. B **84**, 064418 (2011).

[18] H. Ueda, Y. Tanaka, H. Nakajima, S. Mori, K. Ohta, K. Haruki, S. Hirose, Y. Wakabayashi, and T. Kimura, Magnetic structure and effect of magnetic field on its domain structure in magnetoelectric $Ba_{1.3}Sr_{0.7}CoZnFe_{11}AlO_{22}$, Appl. Phys. Lett. **109**, 182902 (2016).

[19] S. Shen, Y. S. Chai, and Y. Sun, Nonvolatile electric-field control of magnetization in a Y-type hexaferrite, Sci. Rep. **5**, 8254 (2015).

[20] T. Nakajima, Y. Tokunaga, M. Matsuda, S. Dissanayake, J. Fernandez-Baca, K. Kakurai, Y. Taguchi, Y. Tokura, and T. Arima, Magnetic structures and excitations in a multiferroic Y-type hexaferrite $BaSrCo_2Fe_{11}AlO_{22}$, Phys. Rev. B **94**, 195154 (2016).

[21] S.-P. Shen, X.-Z. Liu, Y.-S. Chai, A. Studer, K. Rule, K. Zhai, L.-Q. Yan, D.-S. Shang, F. Klose, Y.-T. Liu, D.-F. Chen, and Y. Sun, Hidden spin-order-induced room-temperature ferroelectricity in a peculiar conical magnetic structure, Phys. Rev. B **95**, 094405 (2017).

[22] T. Kimura, Magnetoelectric hexaferrites, Annu. Rev. Condens. Matter Phys. **3**, 93 (2012).

[23] H. Ueda, Y. Tanaka, Y. Wakabayashi, and T. Kimura, Soft x-ray resonant diffraction study of magnetic structure in magnetoelectric Y-type hexaferrite, Physica B **536**, 118 (2018).

[24] H. B. Lee, Y.-S. Song, J.-H. Chung, S. H. Chun, Y. S. Chai, K. H. Kim, M. Reehuis, K. Prokeš, and S. Mat'aš, Field-induced incommensurate-to-commensurate phase transition in the magnetoelectric hexaferrite $Ba_{0.5}Sr_{1.5}Zn_2(Fe_{1-x}Al_x)_{12}O_{22}$, Phys. Rev. B **83**, 144425 (2011).

[25] H. Chang, H. B. Lee, Y.-S. Song, J.-H. Chung, S. A. Kim, I. H. Oh, M. Reehuis, and J. Schefer, Al doping effect on magnetic phase transitions of magnetoelectric hexaferrite $Ba_{0.7}Sr_{1.3}Zn_2(Fe_{1-x}Al_x)_{12}O_{22}$, Phys. Rev. B **85**, 064402 (2012).

[26] T. Takeuchi, A. Chainani, Y. Takata, Y. Tanaka, M. Oura, M. Tsubota, Y. Senba, H. Ohashi, T. Mochiku, K. Hirata, and S. Shin, An ultrahigh-vacuum apparatus for resonant diffraction experiments using soft x rays ($h\nu = 300$–2000 eV), Rev. Sci. Instrum. **80**, 023905 (2009).

[27] L. D. Landau and E. M. Lifshitz, *Quantum Electrodynamics*, 2nd ed. (Pergamon Press, Oxford, 1982), Vol. 4.

[28] S. W. Lovesey and S. P. Collins, *X-ray Scattering and Absorption by Magnetic Materials* (Oxford Science Publications, Clarendon Press, Oxford, 1996).

[29] V. E. Dmitrienko, Forbidden Reflections due to Anisotropic X-ray Susceptibility of Crystals, Acta Cryst. A **39**, 29 (1983).

[30] V. E. Dmitrienko, Anisotropic of X-ray Susceptibility and Bragg Reflections in cubic crystals, Acta Cryst. A **40**, 89 (1984).

[31] J. P. Hill and D. F. McMorrow, X-ray resonant exchange scattering: Polarization dependence and correlation functions, Acta Cryst. A **52**, 236 (1996).

[32] K. Namikawa, M. Ando, T. Nakajima, and H. Kawata, X-ray resonance magnetic scattering, J. Phys. Soc. Jpn. **54**, 4099 (1985).

[33] N. Ishimatsu, H. Hashizume, S. Hamada, N. Hosoito, C. S. Nelson, C. T. Venkataraman, G. Srajer, and J. C. Lang, Magnetic structure of Fe/Gd multilayers determined by resonant x-ray magnetic scattering, Phys. Rev. B **60**, 9596 (1999).

[34] A. M. Mulders, S. M. Lawrence, A. J. Princep, U. Staub, Y. Bodenthin, M. García-Fernández, M. Garganourakis, J. Hester, R. Macquart, and C. D. Ling, Circularly polarized soft x-ray diffraction study of helical magnetism in hexaferrite, Phys. Rev. B **81**, 092405 (2010).

[35] I. A. Sergienko, C. Şen, and E. Dagotto, Ferroelectricity in the Magnetic E-Phase of Orthorhombic Perovskites, Phys. Rev. Lett. **97**, 227204 (2006).

[36] S. Ji, C. Song, J. Koo, K.-B. Lee, Y. J. Park, J. Y. Kim, J.-H. Park, H. J. Shin, J. S. Rhyee, B. H. Oh, and B. K. Cho, Interference of Magnetic and Anisotropic Tensor Susceptibility Reflections in Resonant X-Ray Scattering of GdB_4, Phys. Rev. Lett. **91**, 257205 (2003).

[37] S. Tardif, S. Takeshita, H. Ohsumi, J. Yamaura, D. Okuyama, Z. Hiroi, M. Takata, and T. Arima, All-In-All-Out Magnetic Domains: X-Ray Diffraction Imaging and Magnetic Field Control, Phys. Rev. Lett. **114**, 147205 (2015).

[38] F. Fabrizi, P. A. Thomas, G. Nisbet, and S. P. Collins, Identification of inversion domains in $KTiOPO_4$ via resonant x-ray diffraction, Acta Cryst. A **71**, 361 (2015).

[39] J. W. Cable, E. O. Wollan, W. C. Koehler, and M. K. Wilkinson, Magnetic Structures of Metallic Erbium, Phys. Rev. **140**, A1896 (1965).

[40] W. C. Koehler, J. W. Cable, M. K. Wilkinson, and E. O. Wollan, Magnetic structures of holmium. I. The virgin state, Phys. Rev. **151**, 414 (1966).